

# Vortex shedding from confined micropin arrays

**Journal Article****Author(s):**

Renfer, A.; Tiwari, M. K.; Meyer, F.; Brunswiler, T.; Michel, B.; Poulikakos, D.

**Publication date:**

2013

**Permanent link:**

<https://doi.org/10.3929/ethz-b-000070649>

**Rights / license:**

[In Copyright - Non-Commercial Use Permitted](#)

**Originally published in:**

Microfluidics and Nanofluidics 15(2), <https://doi.org/10.1007/s10404-013-1137-5>

# Vortex shedding from confined micropin arrays

Adrian Renfer · Manish K. Tiwari ·  
Ferdinand Meyer · Thomas Brunschwiler ·  
Bruno Michel · Dimos Poulikakos

Received: 27 September 2012 / Accepted: 7 January 2013 / Published online: 23 January 2013  
© Springer-Verlag Berlin Heidelberg 2013

**Abstract** The hydrodynamics in microcavities populated with cylindrical micropins was investigated using dynamic pressure measurements and fluid pathline visualization. Pressure signals were Fourier-analyzed to extract the flow fluctuation frequencies, which were in the kHz range for the tested flow Reynolds numbers ( $Re$ ) of up to 435. Three different sets of flow dependent characteristic frequencies were identified, the first due to vortex shedding, the second due to lateral flow oscillation and the third due to a transition between these two flow regimes. These frequencies were measured at different locations along the chip (e.g. inlet, middle and outlet). It is established that vortex shedding initiates at the outlet and then travels upstream with increase in  $Re$ . The pathline visualization technique

provided direct optical access to the flow field without any intermediate post-processing step and could be used to interpret the frequencies determined through pressure measurements. Microcavities with different micropin height-to-diameter aspect ratios and pitch-to-diameter ratios were tested. The tests confirmed an increase in the Strouhal number (associated with the vortex shedding) with increased confinement (decrease in the aspect ratio or the pitch), in agreement with macroscale measurements. The compact nature of the microscale geometry tested, and the measurement technique demonstrated, readily enabled us to investigate the flow past 4,420 pins with various degrees of confinements; this makes the measurements performed and the techniques developed here an important tool for investigating large arrays of similar objects in a flow field.

**Electronic supplementary material** The online version of this article (doi:10.1007/s10404-013-1137-5) contains supplementary material, which is available to authorized users.

**Keywords** Flow pathline visualization · Microscale flows · Vortex shedding · Strouhal number · Confinement effect

A. Renfer · M. K. Tiwari · F. Meyer · D. Poulikakos (✉)  
Department of Mechanical and Process Engineering,  
ETH Zurich, 8092 Zurich, Switzerland  
e-mail: dimos.poulikakos@ethz.ch;  
dimos.poulikakos@sl.ethz.ch

A. Renfer  
e-mail: arenfer@ethz.ch

M. K. Tiwari  
e-mail: mtiwari@ethz.ch

F. Meyer  
e-mail: maxmeyer@student.ethz.ch

T. Brunschwiler · B. Michel  
Advanced Thermal Packaging, IBM Research-Zurich,  
8803 Rueschlikon, Switzerland  
e-mail: tbr@zurich.ibm.com

B. Michel  
e-mail: bmi@zurich.ibm.com

## 1 Introduction

Hydrodynamics of flow past obstacles confined in microcavities is relevant to a variety of microfluidic applications such as microfluidic memory and control elements (Groisman et al. 2003), micro-reactors (Moghtaderi 2007), electronics cooling (Renfer et al. 2011) and microporous media (Sen et al. 2012). From the fluidics point of view, flows past such micropin arrays are particularly interesting. Unlike flow through a microchannel, where hydrodynamic transition from laminar to turbulent flow occurs at relatively high Reynolds numbers ( $Re$ ), a complex flow transition in confined micropin arrays triggers unstable flow phenomena even at low  $Re$ . The understanding of the fluid dynamics in micro-total analysis systems ( $\mu$ TAS) and in

fluid based microelectromechanical systems (MEMS) relies on the advances in microscale flow visualization and characterization to improve the device efficiency (Osman et al. 2012). Also within the growing field of lab-on-chip applications it is important to understand the detailed flow distribution in microchannel networks (Gunther and Jensen 2006). Flow visualization in microfluidic systems is clearly emerging as an interdisciplinary technology driving scientific achievements in various research fields, such as single-cell biomechanical perfusion systems (Rossi et al. 2009), microscale pumping technologies (Nabavi 2009), mass transfer enhancement using chemical micro-mixers (Hoffmann et al. 2006; Chung et al. 2004), mixing of fluids in microchannels (Stroock et al. 2002) and cooling of 3D integrated electronics (Renfer et al. 2011) to name but a few. With respect to the latter, there is a clear impact of fluid dynamics on heat transfer in integrated devices: with the advancing miniaturization of high power density electrical devices, liquid based cooling solutions will become a conceivable strategy in the near future. Especially, for compact systems as concentrated photovoltaics, power amplifiers and integrated circuits, the fluidics and related cooling at the microscale and nanoscale are becoming a crucial technology to further improve their performance. To exemplify, the concept of integrated water cooling has received much attention (Brunschwiler et al. 2009; Dang et al. 2010; Alfieri et al. 2012). Given the clear coupling of thermal transport with fluidics, the investigation of the detailed flow behavior is of paramount importance.

Whereas numerous studies are devoted to macroscopic cylinder arrays (Ziada 2006; Sweeney and Meskell 2003), fluidics aspects involved in the corresponding microscale analog of flow past cylindrical arrangements have rarely been addressed in the literature. The compact nature of the microfluidic geometry allows fitting, several thousands of confined micropins in a small area. Such high numbers are unparalleled compared to macroscopic tube bundles, which also do not contain the confinement effect of their microscopic counterparts. Our results herein show that large micropin arrays furnish transient effects and multiple flow fluctuation frequencies. Flow fluctuations in macro-flow geometries are measured by means of hot-wire and Laser Doppler Anemometry (LDA) techniques that require either direct contact of the probe with the flow or sufficiently large optical access. Visualization methods in general require high intensity light sources and fast charge coupled device (CCD) cameras to capture the fluid dynamics with a high temporal resolution. This is required since vortex-induced flow field fluctuations in tube arrays range from a few Hz up to several hundreds of Hz.

For the hydrodynamic investigation of flow through micropin arrays, on the other hand, standard experimental techniques cannot be applied. Therefore, the development of

novel measurement approaches that are specifically targeted to microfluidics is clearly warranted. The frequency of vortex shedding in micropin arrays is one order of magnitude higher compared to the macroscopic pendant and in combination with the inevitably low illumination conditions in microstructures, direct observation of unsteady flow processes remains challenging. Even state-of-the art micro-particle image velocimetry ( $\mu$ PIV), one of the most sophisticated visualization techniques for microscale flows, is unable to resolve the full dynamic picture of kHz frequency flow fluctuations. The two-frame cross-correlation technique in  $\mu$ PIV resolves flow processes with a high temporal resolution in the microsecond time scale to instantly freeze flow fluctuation patterns in microcavities (Natrajan and Christensen 2010; Renfer et al. 2011). The limitation, however, is given by the slow repetition frequency of a few Hz for state-of-the art intensified CCD cameras and consequently the unsteady dynamics of the flow cannot be captured. Use of dynamic pressure sensors is an attractive option to capture the flow fluctuation frequencies and the corresponding dynamics. However, contrary to large scale tube bundle measurements, microscale flow fluctuations introduce only a small disturbance to the pressure oscillations that are also inevitably present in any external pump driven flows. Therefore, an accurate and systematic experimental methodology needs to be developed to distinguish the fluidic fluctuations from the system noise.

Based on the above, the flow visualization and quantitative assessment of the microfluidics involved in flow past confined arrays of micropins is the main focus of our work. To this end, first the measured dynamic pressure helped quantify the vortex-induced fluctuations; the frequency of flow fluctuations was established to be in the kHz regime. In addition, to corroborate the results from the pressure sensor, a new large field-of-view optical technique is introduced to visualize unsteady microscale flows. The technique relies on using scattered light from the seed particles in the flow and is realized by modifying a commercial  $\mu$ PIV setup. The technique enabled us to accurately capture the flow fluctuation and vortex dynamics in flows past confined arrays of micropins. Consequently, the flow fluctuation frequency was determined independently through dynamic pressure measurements including frequency domain analysis of the pressure signal and flow field analysis. A good agreement was obtained between the flow fluctuations of visualization and pressure measurements. Our investigation provides a new way to investigate unsteady flows in microfluidic systems with fluctuation frequencies up to tens of kHz. While the focus of this work is entirely on the fluidic aspect of vortex shedding and flow fluctuations in basic arrays of microscale geometries, the presented microfluidic chips could simulate the fluidic behavior a single layer in interlayer cooling structures for three-dimensional electronic chip stacks.

## 2 Experimental section

### 2.1 Microfluidic chip fabrication

The microfluidic chips were prepared using standard micro-fabrication techniques. Figure 1a and b shows the pictures and the schematics of the chips used in the study, respectively. The cylindrical micropins as well as the fluid ports were etched into silicon with deep reactive ion etching (DRIE) followed by anodic bonding of a 500 μm thick glass plate to the top of the chip to seal the cavity. The glass plate allowed optical access for flow visualization. The resulting microfluidic chip cavity was square shaped in top-view (10 × 10 mm<sup>2</sup>) and two different chip cavity heights of 200 and 100 μm were tested. The chip had four pressure ports located along the cavity edge at 0, 1, 5, and 10 mm in flow direction (see Fig. 1a). However, for our measurements only two ports were used to investigate the pressure fluctuations along the flow direction. The port at 1 mm was used to measure the pressures at the chip inlet and outlet (by reversing the flow direction), and the port at 5 mm was used for the measurement in the middle of the chip. The pressure ports were all identical and reached into the cavity as shown in the scanning electron microscope (SEM) image in the inset of Fig. 1a. The chip cavity was connected to a water tank using two rectangular 1 × 10 mm<sup>2</sup> inlet and outlet slots.

In total, three different cavity designs with 1,250–4,420 pins in the flow area of the chip were used as shown in Fig. 1b. The first geometry was a fully populated micropin cell with equal transversal and longitudinal pitch ( $p = p_t = p_l$ ); with a pin pitch of 150 μm and a pin diameter  $d = p/2$ . The second set of geometries was a half populated cell arrangement of pins with the same transversal pitch  $p_t = 200$  μm but different longitudinal pitch ( $p_l = 300$  μm and  $p_l = 400$  μm, respectively); both with a

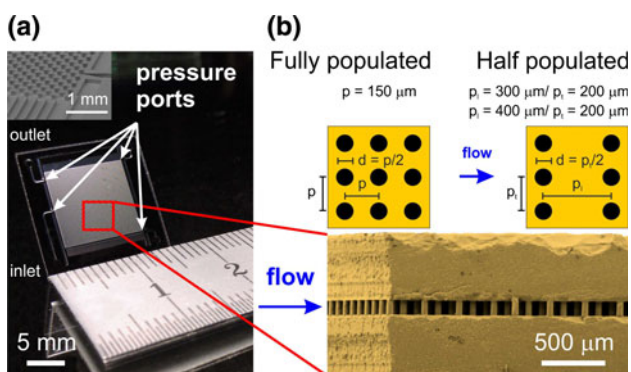
pin diameter of 100 μm ( $d = p_l/2$ ). For the half populated cell, the larger longitudinal pitch reduces the pin density in flow direction.

### 2.2 Measurement method and experimental conditions

Given the low amplitude of the pressure fluctuations in flow past micropins, it was crucial to minimize external flow fluctuations to improve the overall signal quality in micropin arrays.

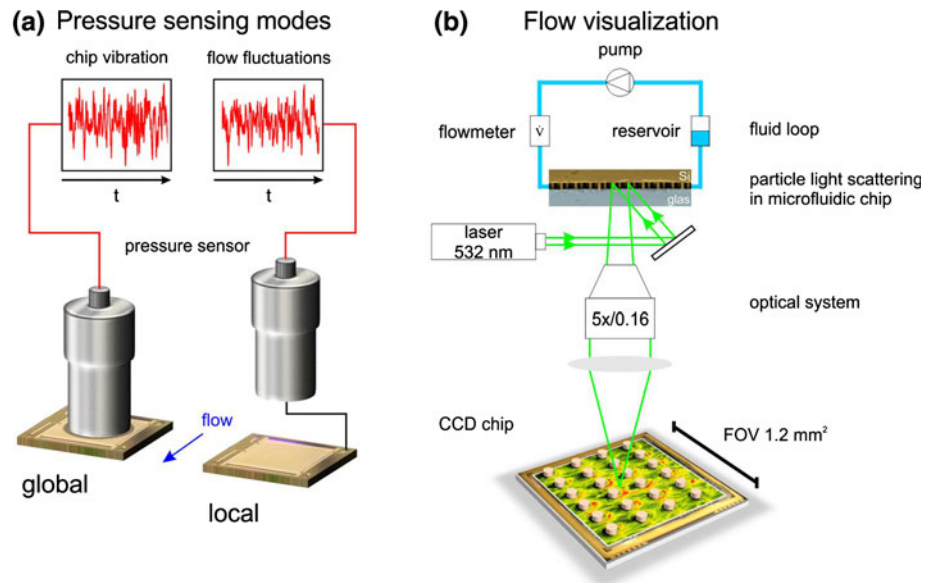
With a home-built pressure-driven flow loop, pump-induced flow fluctuations were almost completely avoided resulting in a highly stable flow rate ( $\pm 0.5$  %, up to 260 ml/min). The flow was measured with a Cubemass DCI Coriolis flow meter (Endress + Hauser, Switzerland) with an accuracy of 0.1 %. The frequency signals were recorded with a dynamic pressure quartz sensor (Kistler, Switzerland) connected to the pressure ports for local pressure sensing and in contact with the chip cover glass for a global measurement (sensor diameter 9.5 mm), respectively (see Fig. 2a). The natural frequency of the dynamic pressure sensor given by the manufacturer is around 70 kHz, which permitted frequency measurements up to  $\sim 25$  kHz ( $\sim 1/3$  of the natural frequency). The signals were low-pass filtered, at 30 kHz, for anti-aliasing, before recording at a sample rate of 100 kHz to fulfill the Nyquist criterion. Fast Fourier transformation (FFT) was used to express the time series in the frequency domain to analyze the dominant frequencies. With a total sampling time of 500 ms, a frequency resolution of 2 Hz is achieved. Since the flow fluctuation frequency regime investigated ranges from 3 to 14 kHz, the relative frequency resolution of the signal acquisition system is  $< 0.07$  %. Each frequency peak for a given Reynolds number was calculated by averaging 20 data sets in the frequency domain; each calculated from the FFT of the pressure signal acquired over a time interval of 500 ms. This results in a flow fluctuation frequency peak obtained over a time period of 10 s. There was a readout delay of  $\sim 1$  s between individual 500-ms data sets. Averaging multiple frequency signals reduces random noise and only frequencies stable in time will withstand such an ensemble signal conditioning, thereby improving the signal to noise ratio.

Figure 2b shows the fluid loop and the optics used for flow visualization. In the visualization experiments, the flow was driven with a magnetically coupled gear pump (Fluidotech, Italy) and the flow rate was measured with a laminar pressure gradient flow sensor (range: 0–500 ml/min, full scale accuracy of 2 %, Omega, USA). The optical setup consisted of an epifluorescent microscope system used for  $\mu$ PIV (FlowMaster Mitas, LaVision, Goettingen, Germany) with a modified sample illumination to image



**Fig. 1** **a** Photograph and SEM image of the microfluidic chip with the pressure ports and inlet/outlet slots indicated. **b** Schematic of the chips with fully and half populated micropin arrays. The different pitch values used are also shown (top) with an SEM image of the micropins in the flow cavity (bottom)

**Fig. 2** **a** Local and global sensing modes were applied to measure the fluctuating pressure of micropin cavities. **b** Schematic of the particle scattering flow visualization system with the microfluidic chip connected to a water loop



the light scattered by particles seeded into the flow. By altering the exposure time of the camera, the pathlines of the seeded particles could be recorded. The micropin array chips were placed on the  $x$ - $y$ - $z$  stage of the setup to change the location of the observed (focused) area. Seeding the flow with silver-coated polystyrene particles (4.2  $\mu\text{m}$  in diameter, microparticles GmbH, Berlin, Germany) enhanced the scattering intensity compared to non-reflective particles. The tracer particles were illuminated with a continuous 532 nm DPSS Nd:YAG laser (300 mW, CrystaLaser, Reno, USA) and the scattered light was recorded with a  $2,048 \times 2,048$  pixel intensified CCD camera. A  $5\times$  microscope objective ( $\text{NA} = 0.16$ ) was used providing a quadratic  $1.2 \text{ mm}^2$  field-of-view. The grayscale visualization images were rescaled with a green color scale for better visibility of the pathlines. With the pathline visualization technique it is possible to visualize the trajectory of a tracer particle and, therefore, the fluid path is seen directly without any intermediate correlation method, which, in contrast, is required for  $\mu\text{PIV}$ . In addition, to produce qualitative flow patterns, the tracer particle density can be significantly lowered to reduce the measurement complexity (e.g. mitigation of clogging). All measurements were conducted at room temperature with de-ionized (DI) water as the working fluid.

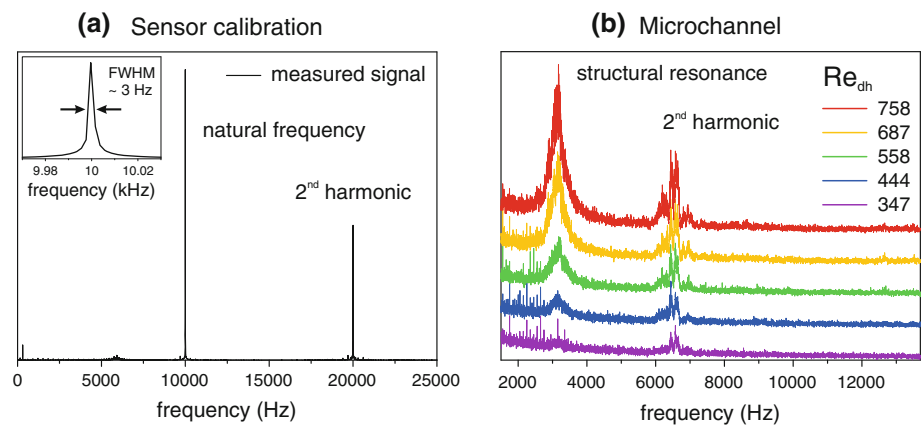
### 2.3 Frequency validation

Three distinct procedures were used to ensure the accuracy and validate the frequency results obtained using pressure measurements and visualization of flow fluctuations in a micropin array. The latter investigation will be presented in Sect. 3.

The pressure sensor calibration ensures an accurate frequency read-out including signal conditioning. Figure 3a shows the FFT spectrum of the signal from the pressure sensor fitted to a vibration exciter (type 4809, Brüel & Kjær, Bremen, Germany) with a fundamental natural frequency of 10 kHz. The sensor signal was acquired with the presence of the adapter (needed for local port pressure measurements as seen in Fig. 2a) to simulate actual experiments. The sharp frequency peak at 9.9996 kHz with a full width at half maximum (FWHM) of 3 Hz (inset in Fig. 2a) establishes the good accuracy of the pressure sensor including the signal conditioning procedure. The peak at  $\sim 20$  kHz is the second harmonic of the exciter.

In the flow regime investigated, vortex-induced pressure fluctuations are expected to be a linear function of the Reynolds number, resulting in a constant Strouhal number. Therefore, hydrodynamic frequencies can be distinguished from the inevitably present structural resonant frequencies of the chips by changing the flow rate. The presence of structural vibration was confirmed by performing separate measurements on chips with microchannels filling the microcavity. Unlike in the case of micropin arrays, we do not expect to observe any vortices in the microchannel configuration. This fact can serve as an additional confirmation to the frequency measurements reported for flow past micropin arrays. Therefore, global vibration measurements (see Fig. 2a) were conducted with a microchannel chip ( $p = 200 \mu\text{m}$ ,  $h = 200 \mu\text{m}$ ). As expected, the results presented in Fig. 3b only show the structural frequencies that lack any dependence on  $Re$ , which is a unique feature of the hydrodynamic frequencies recorded from micropin chips (discussed below). Within the measurement error, Fig. 3b only captures two modes of the structural

**Fig. 3** **a** The calibration spectrum shows the accuracy of the dynamic pressure sensor used for flow fluctuation measurements. The sensor was excited using an exciter with a fundamental natural frequency of 10 kHz. **b** FFT spectra are plotted to show structural frequencies in a microchannel geometry where no Reynolds number dependent frequency is expected to exist



frequencies; the fundamental mode at  $\sim 3.2$  kHz and the second harmonic at  $\sim 6.5$  kHz. The random disturbances originating at the inlet and outlet of the chip are responsible for exciting these structural modes of vibration, which were present in all our measurements, although not at exactly the same frequencies given the variation in the geometries of the different chips used.

### 3 Results and discussion

#### 3.1 Fluctuating pressure measurements

Dynamic pressure fluctuation and the corresponding FFT spectra for the half-populated micropin array with height  $h = 200 \mu\text{m}$  and pitch  $p_1 = 300 \mu\text{m}$  were measured at the inlet and outlet, in the middle and with the sensor on top of the chip. The measurements cover a Reynolds number (based on pin diameter) range up to 435 at a pressure drop of 1.4 bar across the whole chip. The waterfall plots in Fig. 4 show a set of frequency curves at different Reynolds numbers. The figure presents the results of local measurements near inlet, outlet and the middle and global (contact) measurements. The latter clearly shows some peaks originating from structural vibrations akin to the microchannel chip although the exact location of the peaks varies. Arbitrary scales have been used to clearly delineate the location of the peaks in the figure. The flow fluctuations were found to be highly stable in time. This becomes clear if we consider that our reported peaks were averaged over 20 measurements each with a signal span of 500 ms. The total time (10 s), for example, corresponds to nearly 80,000 flow oscillations at a frequency of  $\sim 8$  kHz. For each of these oscillations the observed full width at half maximum (FWHM) was  $\sim 100$  Hz demonstrating transient stability of the oscillations in our signal.

The FFT spectra in Fig. 4 show three  $Re$  dependent frequency components. As the frequencies varied linearly

with  $Re$ , they were assigned to three Strouhal numbers  $St_{\text{low}}$ ,  $St_{\text{med}}$  and  $St_{\text{high}}$  defined as

$$St = fd/u_{\text{flow}},$$

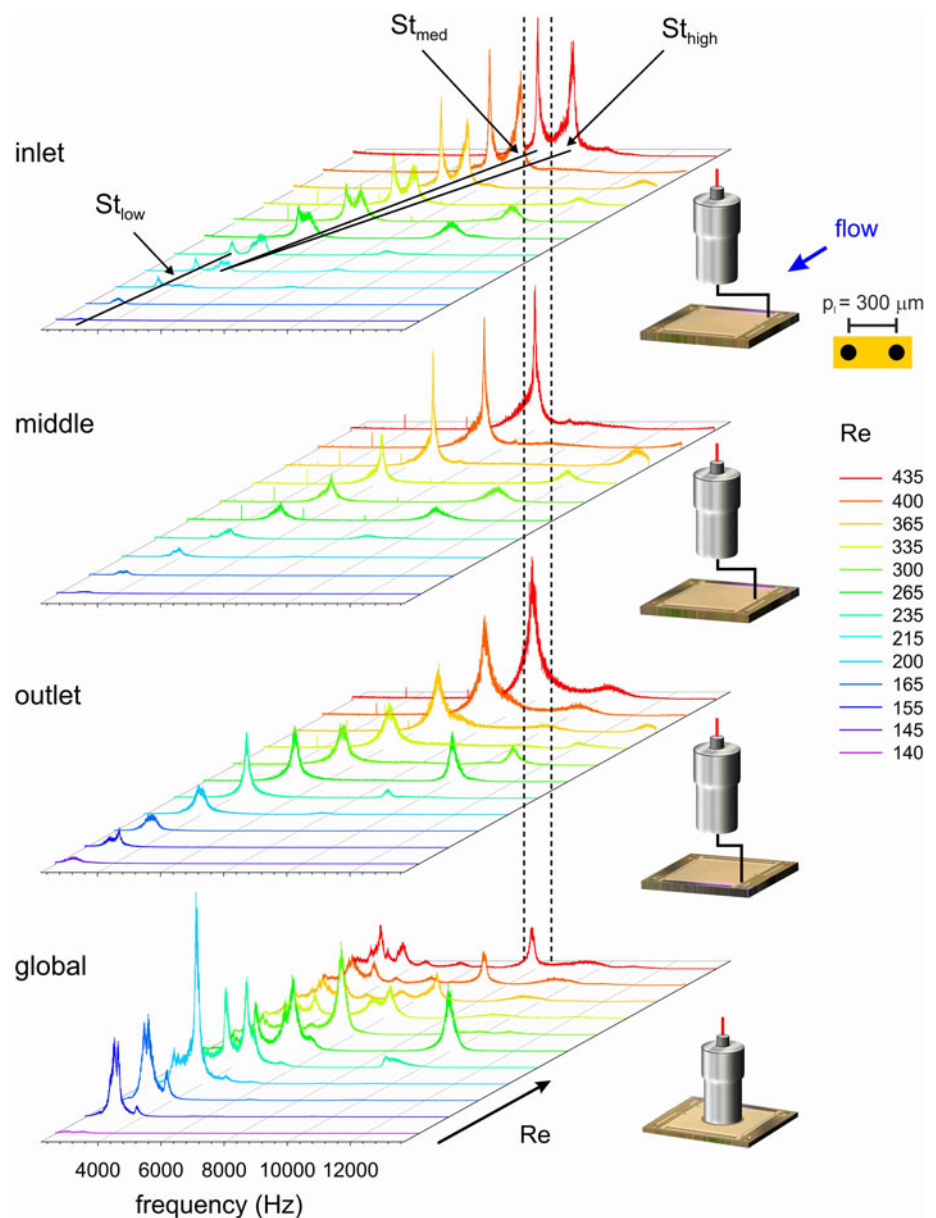
which is expressed in terms of the pin diameter  $d$  and the mean velocity of the fluid  $u_{\text{flow}}$  between the pins. Clearly, the Strouhal number can be conveniently calculated from the experimentally measured frequencies and the mean fluid velocities.

Before analyzing the fluctuation frequencies, it is important to understand the presence and influence of structural (flow independent) frequencies. This will help explain the origin of the occasional rightmost peaks in some spectra, see for example the green curves at  $Re = 265$  and  $300$  in the inlet plot of Fig. 4.

The benefit of the global contact measurements is that they also capture the structural frequencies. Figure 5 shows in detail the global mode measurement from Fig. 4 with the different frequencies highlighted. Since the sensor was in direct contact with the chip, the measurements captured the device related vibrations. The first structural frequency peak occurs at  $\sim 3.5$  kHz (close to the microchannel vibration in Fig. 3b). At the onset of flow fluctuations, the measured pressure fluctuation frequency occurred close to the structural frequency and, consequently, was amplified via resonance as indicated in the gray shaded region of Fig. 5 (amplified hydrodynamic peak).

This explains the high amplitudes observed at low  $Re$ . With the increase in  $Re$  the hydrodynamic frequency gradually increases beyond the structural frequency, becomes distinct and therefore its amplitudes decrease. Occasionally, however, the higher harmonics of the hydrodynamic frequency coincides with higher harmonics of the fundamental structural vibration (outside the gray shaded region in Fig. 5). This leads to their amplification through resonance (e.g. the amplified 2nd harmonic at  $Re = 265$  in Fig. 5). Therefore, the global measurements, which clarify the location of structural frequencies, help us

**Fig. 4** Frequency spectra of the pressure fluctuations measured at different locations for a micropin array with  $p_1 = 300 \mu\text{m}$  and  $h = 200 \mu\text{m}$ . At the inlet and middle port, three distinct frequencies emerged with corresponding Strouhal number  $St_{\text{low}}$ ,  $St_{\text{med}}$  and  $St_{\text{high}}$  (best visible at the inlet, highlighted with *solid lines*).  $St_{\text{high}}$  was not observed at the outlet and with the global sensing mode only the dominant medium frequency was measured (indicated with *dashed lines* at the inlet, middle, outlet and in global mode for  $Re = 435$ )



in understanding the occasional amplification in the flow dependent harmonics of the flow fluctuation peaks.

The three different sets of flow dependent fluctuation frequencies  $f_{\text{low}}$ ,  $f_{\text{med}}$  and  $f_{\text{high}}$  in Fig. 4 are best visible in the spectra measured at the inlet port. The low frequency peak at the inlet was measured up to  $Re = 235$ , whereas a high frequency component emerged at  $Re = 215$ . These peaks correspond to Strouhal numbers  $St_{\text{low}}$  and  $St_{\text{high}}$ , respectively. In addition, a dominant medium frequency with  $St_{\text{med}}$  was observed at all local pressure ports as well as in the global measurement (see Fig. 4). The three different fluctuation frequencies were also observed at the middle port of the micropin array. At the middle, however, the signal intensity of the medium frequency was

clearly higher than the amplitudes of  $f_{\text{low}}$  and  $f_{\text{high}}$ ; at the outlet,  $St_{\text{high}}$  was completely absent. Figure 6a shows the observed frequencies in the micropin array  $f_{\text{low}}$ ,  $f_{\text{med}}$  and  $f_{\text{high}}$  plotted together as a function of  $u_{\text{flow}}$ . Clearly the data collapse on three different straight lines. The corresponding Strouhal numbers  $St_{\text{low}}$ ,  $St_{\text{med}}$  and  $St_{\text{high}}$  are shown in Fig. 6b.

As noted above, due to their high sensitivity, the low signal fluctuations corresponding to  $St_{\text{low}}$  and  $St_{\text{high}}$  were only detected by the local measurements. Therefore, the dominant frequency in the micropin array corresponds to  $St_{\text{med}}$ . The source of  $f_{\text{high}}$  is vortex-induced flow fluctuations as will become clear after the flow visualization presented later.

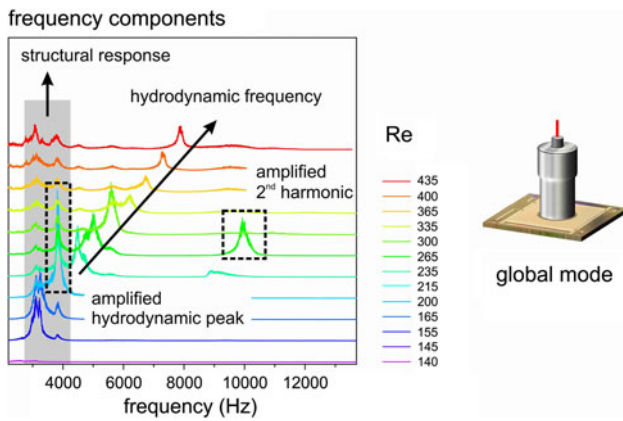


**Fig. 5** In global mode, three different excitation mechanisms were found. The first mode of structural vibrations was sensed at ~3.5 kHz. The *Re* dependent hydrodynamic peaks and their occasionally visible higher harmonics are enhanced via resonance when their corresponding frequency coincides with the first structural mode or its higher harmonics

### 3.2 Effect of confinement on the vortex shedding frequency

Devices developed with microfabrication technologies benefit from compact designs allowing the integration of high functional density systems into small package dimensions. Integrated water-cooled electronic packages need through-silicon-vias (TSV) as communication pathways between vertically stacked processors. The embedded microfluidic cavities required to remove the dissipated heat, introduce additional layers between stacked processors increasing the length of the TSV. Therefore, it is important to understand the influence of both the TSV number density and the aspect ratio on the flow behavior. To this end, the microcavities with micropins used in this work could be thought to simulate a single fluidic layer with micropins representing the TSV. To investigate the effect of confined flow through such an array, two different

confinement configurations are studied and analyzed in the following subsections.

#### 3.2.1 Changing micropin density

It is obvious that the highest electrical interconnect densities are achieved by reducing the distance between individual TSVs. To clarify the effect of the resulting horizontal confinement on the Strouhal number, flow fluctuation measurements on three different micropin arrays with cavity heights  $h = 200 \mu\text{m}$  were compared. The horizontal confinement can be conveniently characterized using the ratio of longitudinal pitch-to-pin diameter ( $p/d$ ). In Fig. 7a, the dominant frequencies ( $f_{\text{med}}$ ) are plotted against the mean fluid velocity and the corresponding Strouhal numbers are presented in Fig. 7b. For a given mean fluid velocity, the curves in Fig. 7a show that the flow fluctuation frequency was higher for a smaller longitudinal pitch. This shows that the increase in the longitudinal confinement between micropins shifts the vortex shedding to higher frequencies. With increasing  $p/d$  ratio the Strouhal number is observed to clearly decrease (Fig. 7b). This is in agreement with macroscopic tube bundle measurements where the Strouhal number was reported to decrease with increasing  $p/d$  ratios (Owen 1965; Weaver et al. 1987; Polak and Weaver 1995).

#### 3.2.2 Vertical confinement

While high packaging densities and short TSVs are preferred for integrated water-cooled electronics, the reduced cavity height is expected to affect the flow behavior significantly. For the macroscale geometries, increasing the vertical confinement of single rectangular cylinders was found to delay the onset of vortex shedding and also to increase the Strouhal number as reported in experimental and numerical studies (Davis et al. 1984; Turki et al. 2003;

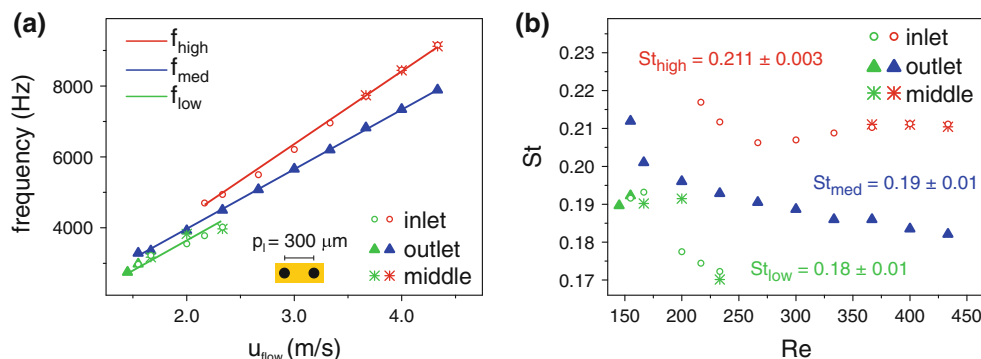


**Fig. 6** **a** Different sets of flow fluctuation frequencies were detected in an inline micropin array ( $h = 200 \mu\text{m}$ ,  $p_1 = 300 \mu\text{m}$ ) with the corresponding Strouhal numbers indicated. **b** The frequencies clearly

correspond to three different Strouhal numbers  $St_{\text{low}}$ ,  $St_{\text{med}}$  and  $St_{\text{high}}$ . The data are adopted from the local measurements at the inlet, outlet and middle of the chip (see Fig. 4)

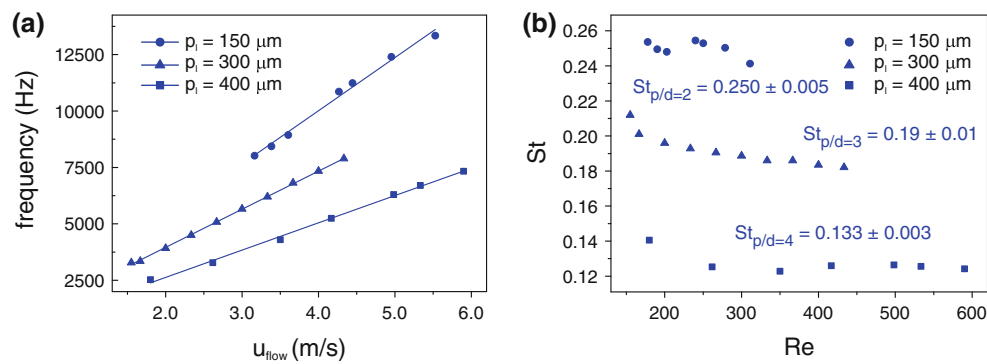
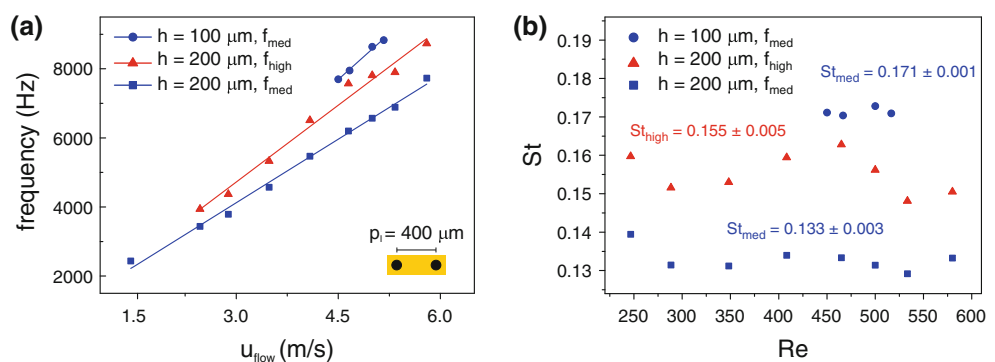


**Fig. 7** **a** Frequency curves and **b** Strouhal numbers for 200  $\mu\text{m}$  high microcavity chips with different pitch-to-diameter ratios demonstrating the role of horizontal confinement on the vortex shedding frequency and the Strouhal number, respectively

Patil and Tiwari 2010). For micropin arrays, using  $\mu\text{PIV}$  we previously reported that the reduction in aspect ratio suppresses the vortex shedding for a cavity height  $h = 100 \mu\text{m}$  up to  $Re = 330$ , whereas vortex shedding for the same pin diameter but with  $h = 200 \mu\text{m}$  already started at  $Re = 200$  (Renfer et al. 2011). To clarify whether the Strouhal number for micropin arrays is increased in the presence of confining walls, frequency spectra were obtained for chips with  $h = 100 \mu\text{m}$  and  $h = 200 \mu\text{m}$ , respectively. The resulting frequencies are plotted in Fig. 8a as a function of  $u_{\text{flow}}$ . For both chips  $p_1$  was kept at  $400 \mu\text{m}$ . With a cavity height  $h = 200 \mu\text{m}$ , a higher and a medium frequency component with  $St_{\text{high}} = 0.155$  and  $St_{\text{med}} = 0.133$  was measured (see Fig. 8b). For  $h = 100 \mu\text{m}$ , i.e., aspect ratio  $h/d = 1$ , only a single Strouhal number  $St_{\text{med}} = 0.171$  was found, in the  $Re$  range investigated. The  $Re$  range was decided by the high pressure drop across the chip, which limited the range of frequency measurements. For a given  $Re$ , however, the dominant flow fluctuations ( $f_{\text{med}}$ ) in the chip with a low aspect ratio cavity  $h/d = 1$  occurred at significantly higher frequencies compared to the ones with  $h/d = 2$ .

The vertical confinement not only influenced the shedding frequency but also delayed the onset of vortex shedding. Figure 8b shows clearly the difference between the onsets of vortex shedding for distinct aspect ratio cavities.

**Fig. 8** **a** Frequency curves for micropin arrays for two different cavity heights and equal pitch  $p_1 = 400 \mu\text{m}$ . **b** For  $h/d = 2$ , two Strouhal numbers were observed while for  $h/d = 1$  the onset of vortex shedding was delayed and the flow fluctuations occurred at higher frequencies

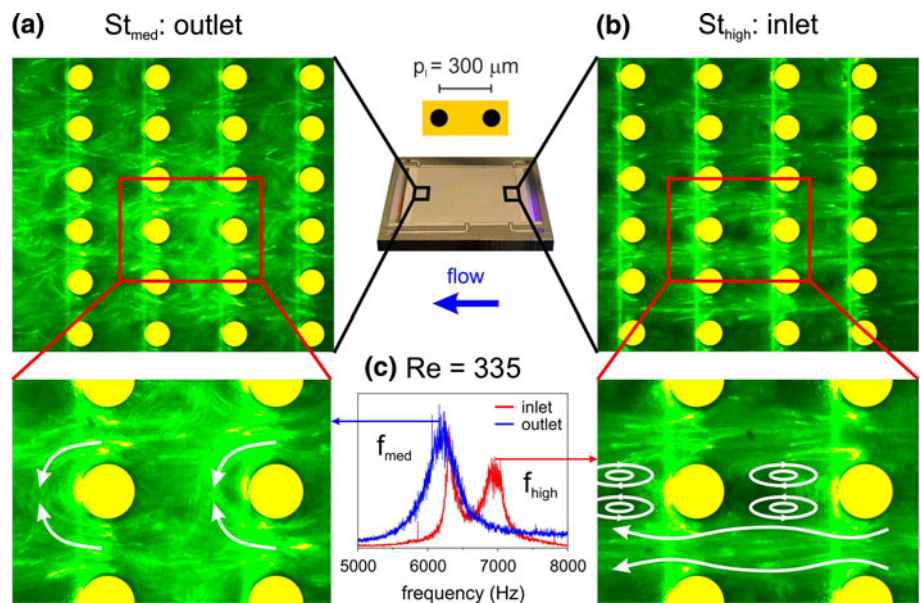


The reason for this can be understood as follows. It is known that once vortex shedding is triggered, stagnant recirculation zones between successive micropins collapse and the gap flow (flow through the gap between the pins in the lateral direction) penetrates the space in between the pins (Renfer et al. 2011). For the geometry with  $h/d = 1$ , i.e. for a lower aspect ratio, the flow is more confined between the cavity walls than for the one with  $h/d = 2$ , thereby stabilizing steady recirculation zones and inevitably affecting the formation of flow fluctuations. As a result the onset of vortex shedding is delayed until higher  $Re$  for lower aspect ratios.

### 3.3 Visualization of flow fluctuations

To better understand the fluid dynamical origin of the measured flow fluctuation frequencies, particle pathline visualization was performed at the inlet and outlet for the chip with  $p/d = 3$ , which was also used for the measurements in Fig. 4. The height of the cavity was  $h = 200 \mu\text{m}$  and it was filled with pins  $d = 100 \mu\text{m}$ . As mentioned above, it is known that in the absence of any flow fluctuations, stagnant symmetric pairs of vortices form in the wake of the micropins. These recirculation zones collapse and vortices are shed from the micropin causing flow impingement. The vortex shedding and the associated flow

**Fig. 9** Pathline visualization at the inlet and outlet for  $Re = 335$  to clarify the origin of the flow frequencies and Strouhal numbers  $St_{med}$  and  $St_{high}$ , respectively. **a** Karman vortex shedding induced flow impingement at the outlet occurred with  $St_{med}$ , whereas **b** at the inlet, recirculation zones between the micropins are stable with time. The averaged flow pathlines are highlighted with the *sinusoidal arrows*. **c** Small amplitude flow fluctuations between the micropins at the inlet induce a measurable frequency component  $f_{high}$ . The vortex shedding frequency  $f_{med}$  was recorded at the outlet



impingement are initiated via small perturbations that induce the gap flow to oscillate within the confined space between the micropins. In our visualizations, we see fully established Karman vortex shedding at the outlet (Fig. 9a) and a pretransition flow with small amplitude oscillations at the inlet (Fig. 9b) for a flow  $Re = 335$ . Figure 9c compares the frequencies at  $Re = 335$  from Fig. 4, both at the inlet and outlet.

The established vortex shedding at the outlet is in sync with the pressure drop measurements, which indicate that the vortex shedding started at  $Re = 125$  (not shown for brevity). Once vortex shedding is initiated at the outlet, no steady recirculation zones were observed anymore as the flow alternately penetrated the space between the micropins. In the frequency spectrum at the outlet, for  $Re = 335$  only the medium frequency component  $f_{med}$  was measured and therefore, it was assigned to vortex shedding as visualized in Fig. 9a.

From the FFT spectra obtained at different locations along the chip (Fig. 4), it was evident that the high frequency signal  $St_{high}$  emerged with highest amplitude at the inlet. The visualization experiments at the inlet presented in Fig. 9b show clearly the absence of strong vortex-induced flow impingement. However, the gap flow between the micropins shows an unsteady behavior marked by a small amplitude lateral oscillation (highlighted with long sinusoidal white arrows in streamwise direction in Fig. 9b). Therefore, the origin of  $St_{high}$  was ascribed to the visualized small amplitude oscillations of the gap flow. Note that the recirculation zones (white ellipses) in Fig. 9b illustrate an averaged flow situation to outline the nearly undisturbed flow between the micropins. Due to the incompressibility of water, however, the dominant medium pressure

oscillation  $St_{med}$  starting downstream was still observed in the FFT spectrum from the inlet measurements (see in Fig. 9c for  $Re = 335$ ). This is a common observation in air tests using microphones (Ziada and Oengören 2000). Two movies prepared from the image sequences of the pathline visualizations (presented in Fig. 9) are available as supplementary material (Online Resource 2 and 3).

In Fig. 6, we also see a series of frequencies corresponding to  $St_{low}$ , which appeared only at low Reynolds numbers. It is speculated that  $St_{low}$  represents a transition flow oscillation from small amplitude lateral fluctuations (corresponding to  $St_{high}$ ) to the vortex shedding led flow impingement (corresponding to  $St_{med}$ ). Note, however, that in the same figure we observe  $St_{high}$  appearing at a much higher  $Re$ . The reason for the latter is primarily related to the limited sensitivity of the pressure sensor. Below a certain threshold flow rate, we expect that the pressure signal is simply not strong enough to be detected and, therefore, our first observation of frequency peak initiates with transitional frequency  $f_{low}$ , followed by the strong peaks which emerge due to onset of vortex shedding at the outlet ( $f_{med}$ ). Furthermore, since the onset of vortex shedding in micropin arrays starts at the outlet and then shifts upstream with increasing  $Re$  (Renfer et al. 2011), at the inlet we observe the  $f_{high}$  peaks corresponding to lateral oscillations at much higher  $Re$  (c.f. frequency plots in Fig. 6a).

Some important differences must be noted between our visualization of microscale pin arrays and the behavior of macroscale cylinder arrays. The first major difference is the large number of cylinders in the array and the flow confinement in low aspect ratio cavities. We believe that these two crucial differences explain the observation of multiple

Strouhal numbers for an inline arrangement. In the macroscale cylinder literature, to the best of our knowledge, only a single Strouhal number has been reported for inline geometries (Ziada 2006). On the contrary, the present inline arrangement results are in closer agreement with multiple Strouhal numbers observed for different tube arrangements like staggered and parallel triangle geometries. Note that the multiple Strouhal numbers found in staggered arrangements (Konstantinidis et al. 2002) and in large  $p/d$  ratio parallel triangle tube bundles (Ziada and Oengören 2000) were lower by a factor of 1.3–1.5. In addition to the obvious difference in the geometry, we believe that the confinement of the cavity has an augmenting effect leading to the higher Strouhal numbers reported in this study. The higher frequency component was observed at the inlet and the lower mode existed deeper inside the bundle, which is in agreement with the present findings.

### 3.4 Optical validation of the flow fluctuation frequency

With the particle pathline visualization, a supplementary direct technique was developed to verify the kHz-pressure fluctuation found from the dynamic pressure measurements.

The micropin geometry with a cavity height of  $h = 100 \mu\text{m}$  and a pitch  $p_1 = 400 \mu\text{m}$  was used to visualize the individual pathlines. From the dynamic pressure measurements presented above, the Strouhal number was  $St_{\text{med}} = 0.171$  for this configuration (Fig. 8b). Pressure drop measurements (not shown for brevity) indicate the onset of vortex shedding at  $Re \sim 350$ . Due to the low pressure fluctuation signal, the shedding frequency was not detectable before  $Re = 450$ . Thus, the shedding frequency  $f_{\text{med}} \sim 6.8 \text{ kHz}$  at  $Re = 400$  was calculated from the experimental Strouhal number  $St_{\text{med}} = 0.171$ . Figure 10 shows the corresponding flow visualizations close to the outlet at  $Re = 400$  at two different exposure times. With an exposure time of  $100 \mu\text{s}$  (Fig. 10a), an optical frequency limit of 10 kHz ( $1/100 \mu\text{s}$ ) was chosen. The transversal fluctuation of the tracer particles does not exceed 10 kHz, as can be seen by the incomplete shedding cycle. The particles moved either upwards or downwards indicating roughly half of the shedding cycle. In Fig. 10b, we see that doubling the exposure time to  $200 \mu\text{s}$  results in a lower optical frequency limit of 5 kHz. The pathlines capture the entire flow fluctuation period simply because with a longer exposure time the subsequent shedding cycles are superimposed on the same image. Therefore, the characteristic time of shedding must lie between 100 and  $200 \mu\text{s}$ , which corresponds to a frequency range of  $5 \text{ kHz} < f < 10 \text{ kHz}$ . This is in excellent agreement with the experimentally extrapolated value of  $f \sim 6.8 \text{ kHz}$ .

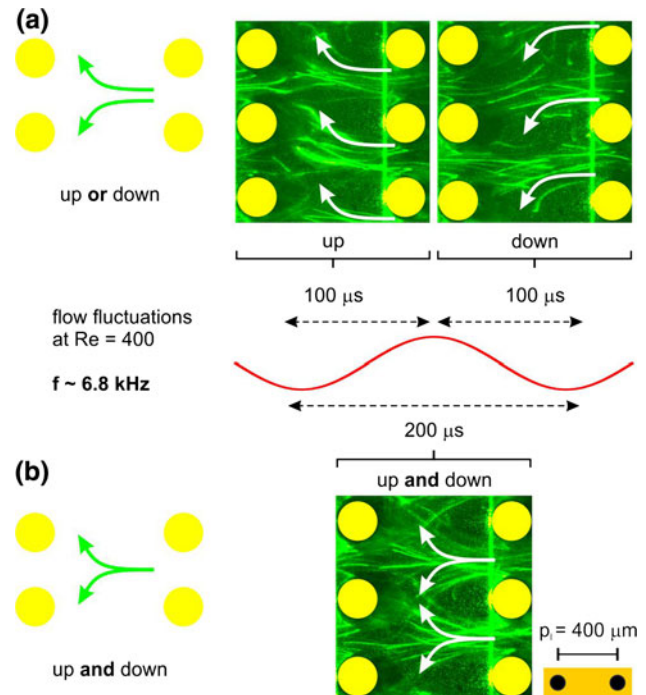


**Fig. 10** Two different exposure times for the visualization images created a lower and upper frequency limit to validate the dynamic pressure sensor measurements. **a** For the upper limit of 10 kHz, incomplete flow cycles were observed with  $t_{\text{exp}} = 100 \mu\text{s}$ . **b** At  $t_{\text{exp}} = 200 \mu\text{s}$  (lower limit of 5 kHz) the entire fluctuation period was captured. This was in agreement with the extrapolated frequency  $f = 6.8 \text{ kHz}$

We attribute the measured dominant fluctuations ( $f_{\text{med}}$ ) to laminar Karman vortex shedding, which is an absolute instability (Monkewitz and Nguyen 1987). However, in the absence of detailed theoretical analysis of the flow instabilities and lack of instrumental sensitivity, it is difficult to ascertain the presence and role of lower order absolute instabilities.

Note that, we have not specifically focused on analyzing the shear layer instabilities in this work. Previous works on flows past macroscale cylinders show a wide range in the value Reynolds number at which shear layer instabilities based on the Kelvin–Helmholtz mechanism are triggered. In flows past macroscopic cylinder arrays, small-scale vortices were reported to form in the shear layer at relatively high Reynolds numbers ( $Re > 7000$ ) (Ziada and Oengören 1992). On the other hand, there are experimental and numerical investigations on flow past single cylinders suggesting shear layer instabilities to appear at Reynolds numbers as low as  $Re \sim 260$  (Prasad and Williamson 1997) or even down to  $Re \sim 50$  (Kumar et al. 2009). However, all these studies point out that the shear layer instabilities are weaker and produce measurement signals with lower strength. Therefore, we believe that in our microscale measurements, with inevitable lower signal to noise ratios

than in the macroscale counter studies, the dominant Karman vortex shedding overshadows the signal from shear layer fluctuations. Moreover, the frequency of unsteady vortices formed in the shear layer scales as  $f \sim Re^{1.67}$  (Prasad and Williamson 1997), whereas the measured fluctuation frequencies in our study vary linearly with  $Re$ . This is understandable, since hydrodynamics in an array of confined micropins is expected to be different due to the large number of pins and pronounced cavity wall damping effects. A clear evidence of this can be seen in the fact that the onset of laminar vortex shedding is delayed to a much higher Reynolds number ( $Re > 150$ ) compared to a single cylinder ( $Re \sim 50$ ). The change should naturally also be reflected in the variation of Strouhal number.

#### 4 Conclusion

This paper presents the effects of microcavities and micropin arrangement confinements on the unsteady hydrodynamics of flows through large arrays of micropins. The results of dynamic pressure measurements revealed Reynolds number dependent fluctuations in the kHz range, which were sensed at pressure ports connected to the microcavity as well as on the surface of the microfluidic chip. Three hydrodynamic frequencies were found. The highest frequency was associated with a lateral oscillation of the flow before the onset of vortex shedding. The vortex shedding frequency was intermediate in Strouhal number and was first detected at the outlet, moving upstream with increase in  $Re$ . The lowest Strouhal number was attributed to a transition frequency, representing an intermediate flow regime between lateral oscillation and fully established vortex shedding. An optical setup was introduced to visualize the flow across the micropins by means of particle pathline visualization. This helped reveal the origin of the flow fluctuations. Small amplitude flow oscillations and Karman vortex-induced fluctuations were observed and attributed to  $St_{high}$  and  $St_{med}$ , respectively. The results demonstrate that the visualization technique is capable to corroborate high pressure frequency measurements. Unlike  $\mu$ PIV, the presented technique allowed the estimation for an upper and lower boundary of the dominant shedding frequency. It was also shown that for microcavities with a height-to-pin diameter ratio of 1, the cavity walls imposed a strong vertical confinement, which delayed the onset of vortex shedding. Moreover, the Strouhal number and the shedding frequency were found to increase with decrease in cavity aspect ratios. A similar effect was observed for the longitudinal confinement of the flow between individual micropins, since the Strouhal number increased with smaller pitch-to-pin diameter ratios.

**Acknowledgments** This work was partially supported by the Swiss Confederation through the SNSF administered RTD project nr. 618\_67-CMOSAIC-funded by Nano-Tera.ch. The support is gratefully acknowledged. AR and MKT also acknowledge the fruitful discussions with Mr. Ashish Asthana and Mr. Fabio Alfieri of LTNT, ETH Zurich.

#### References

- Alfieri F, Tiwari MK, Zinovik I, Brunswiler T, Michel B, Poulikakos D (2012) On the significance of developing boundary layers in integrated water cooled 3D chip stacks. *Int J Heat Mass Tran* 55:5222–5232. doi:10.1016/j.ijheatmasstransfer.2012.05.029
- Brunswiler T, Michel B, Rothuizen H, Kloter U, Wunderle B, Oppermann H, Reichl H (2009) Interlayer cooling potential in vertically integrated packages. *Microsyst Technol* 15:57–74. doi:10.1007/s00542-008-0690-4
- Chung YC, Hsu YL, Jen CP, Lu MC, Lin YC (2004) Design of passive mixers utilizing microfluidic self-circulation in the mixing chamber. *Lab Chip* 4:70–77. doi:10.1039/B310848c
- Dang B, Bakir MS, Sekar DC, King CR, Meindl JD (2010) Integrated microfluidic cooling and interconnects for 2D and 3D chips. *IEEE Trans Adv Packag* 33:79–87. doi:10.1109/Tadvp.2009.2035999
- Davis RW, Moore EF, Purtell LP (1984) A numerical-experimental study of confined flow around rectangular cylinders. *Phys Fluids* 27:46–59. doi:10.1063/1.864486
- Groisman A, Enzelberger M, Quake SR (2003) Microfluidic memory and control devices. *Science* 300:955–958. doi:10.1126/science.1083694
- Gunther A, Jensen KF (2006) Multiphase microfluidics: from flow characteristics to chemical and materials synthesis. *Lab Chip* 6:1487–1503. doi:10.1039/B609851G
- Hoffmann M, Schluter M, Rabiger N (2006) Experimental investigation of liquid–liquid mixing in T-shaped micro-mixers using  $\mu$ -LIF and  $\mu$ -PIV. *Chem Eng Sci* 61:2968–2976. doi:10.1016/j.ces.2005.11.029
- Konstantinidis E, Balabani S, Yianneskis M (2002) A study of vortex shedding in a staggered tube array for steady and pulsating cross-flow. *J Fluid Eng-T ASME* 124:737–746. doi:10.1115/1.1487359
- Kumar B, Kottaram JJ, Singh AK, Mittal S (2009) Global stability of flow past a cylinder with centreline symmetry. *J Fluid Mech* 632:273–300. doi:10.1017/S0022112009007241
- Moghtaderi B (2007) Effect of enhanced mixing on partial oxidation of methane in a novel micro-reactor. *Fuel* 86:469–476. doi:10.1016/j.fuel.2006.08.009
- Monkewitz PA, Nguyen LN (1987) Absolute instability in the near-wake of two-dimensional bluff bodies. *J Fluid Struct* 1:165–184. doi:10.1016/S0889-9746(87)90323-9
- Nabavi M (2009) Steady and unsteady flow analysis in microdiffusers and micropumps: a critical review. *Microfluid Nanofluid* 7:599–619. doi:10.1007/s10404-009-0474-x
- Natrajan VK, Christensen KT (2010) The impact of surface roughness on flow through a rectangular microchannel from the laminar to turbulent regimes. *Microfluid Nanofluid* 9:95–121. doi:10.1007/s10404-009-0526-2
- Osman O, Shintaku H, Kawano S (2012) Development of micro-vibrating flow pumps using MEMS technologies. *Microfluid Nanofluid* 13:703–713. doi:10.1007/s10404-012-0988-5
- Owen PR (1965) Buffeting Excitation of Boiler Tube Vibration. *J Mech Eng Sci* 7:431–439. doi:10.1243/jmes\_jour\_1965\_007\_065\_02
- Patil PP, Tiwari S (2010) Three-dimensional numerical investigations on flow and heat transfer for flow past a channel confined square

- cylinder. *Prog Comput Fluid Dy* 10:146–156. doi:[10.1504/PCFD.2010.033326](https://doi.org/10.1504/PCFD.2010.033326)
- Polak DR, Weaver DS (1995) Vortex shedding in normal triangular tube arrays. *J Fluid Struct* 9:1–17. doi:[10.1006/jfls.1995.1001](https://doi.org/10.1006/jfls.1995.1001)
- Prasad A, Williamson CHK (1997) The instability of the shear layer separating from a bluff body. *J Fluid Mech* 333:375–402. doi:[10.1017/S0022112096004326](https://doi.org/10.1017/S0022112096004326)
- Renfer A, Tiwari MK, Brunschwiler T, Michel B, Poulikakos D (2011) Experimental investigation into vortex structure and pressure drop across microcavities in 3D integrated electronics. *Exp Fluids* 51:731–741. doi:[10.1007/s00348-011-1091-5](https://doi.org/10.1007/s00348-011-1091-5)
- Rossi M, Lindken R, Hierck BP, Westerweel J (2009) Tapered microfluidic chip for the study of biochemical and mechanical response at subcellular level of endothelial cells to shear flow. *Lab Chip* 9:1403–1411. doi:[10.1039/B822270n](https://doi.org/10.1039/B822270n)
- Sen D, Nobes DS, Mitra SK (2012) Optical measurement of pore scale velocity field inside microporous media. *Microfluid Nanofluid* 12:189–200. doi:[10.1007/s10404-011-0862-x](https://doi.org/10.1007/s10404-011-0862-x)
- Stroock AD, Dertinger SKW, Ajdari A, Mezic I, Stone HA, Whitesides GM (2002) Chaotic mixer for microchannels. *Science* 295:647–651. doi:[10.1126/science.1066238](https://doi.org/10.1126/science.1066238)
- Sweeney C, Meskell C (2003) Fast numerical simulation of vortex shedding in tube arrays using a discrete vortex method. *J Fluid Struct* 18:501–512. doi:[10.1016/j.jfluidstructs.2003.08.009](https://doi.org/10.1016/j.jfluidstructs.2003.08.009)
- Turki S, Abbassi H, Nasrallah SB (2003) Effect of the blockage ratio on the flow in a channel with a built-in square cylinder. *Comput Mech* 33:22–29. doi:[10.1007/s00466-003-0496-2](https://doi.org/10.1007/s00466-003-0496-2)
- Weaver DS, Fitzpatrick JA, Elkashlan M (1987) Strouhal numbers for heat-exchanger tube arrays in cross flow. *J Press Vess-T ASME* 109:219–223
- Ziada S (2006) Vorticity shedding and acoustic resonance in tube bundles. *J Braz Soc Mech Sci & Eng* 28:186–189
- Ziada S, Oengören A (1992) Vorticity shedding and acoustic-resonance in an in-line tube bundle part 1: vorticity shedding. *J Fluid Struct* 6:271–292. doi:[10.1016/0889-9746\(92\)90010-Z](https://doi.org/10.1016/0889-9746(92)90010-Z)
- Ziada S, Oengören A (2000) Flow periodicity and acoustic resonance in parallel triangle tube bundles. *J Fluid Struct* 14:197–219. doi:[10.1006/jfls.1999.0259](https://doi.org/10.1006/jfls.1999.0259)